Journal of Materials Chemistry C

RSC Publishing

PAPER

View Article Online
View Journal | View Issue

Cite this: J. Mater. Chem. C, 2013, 1, 7716

Mechanical properties of electrochemically synthesised metal–organic framework thin films†

Ben Van de Voorde,[a] Rob Ameloot,[a] Ivo Stassen,[a] Maarten Everaert,[a] Dirk De Vos*[a] and Jin-Chong Tan*[b]

Received 31st May 2013
Accepted 25th July 2013

DOI: 10.1039/c3tc31039f

www.rsc.org/MaterialsC

We investigated the mechanical properties of metal–organic framework thin-film coatings grown by an electrochemical method, which allows fast deposition in environmentally friendly solvents. For the first time, Cu(CHDA) and $Cu(INA)_2$ are electrochemically synthesised as dense coatings on Cu-electrodes, alongside the well-known $Cu_3(BTC)_2$ (CHDA = *trans*-cyclohexane-1,4-dicarboxylate; INA = isonicotinate; BTC = benzene-1,3,5-tricarboxylate). In order to probe the mechanical behaviour of the MOF coatings, both nanoindentation and nanoscratch experiments are performed. The indentation of a polycrystalline film allows the determination of average Young's moduli and hardness of the coatings. Cu(CHDA) exhibits the highest stiffness and hardness, with values of 10.9 GPa and 0.46 GPa, respectively. Intermediate values are obtained for the well-known $Cu_3(BTC)_2$ and the smallest values for $Cu(INA)_2$. A close inspection of the crystal lattice of the MOF materials under investigation allows for correlating the mechanical properties and structural building units of these materials. Finally, the effect of the fundamental mechanical properties of MOF films on their scratch and wear resistance is illustrated.

1 Introduction

Metal–organic frameworks (MOFs) are a hybrid class of crystalline materials, combining both inorganic and organic building blocks.[1] They offer a unique range of properties such as framework flexibility,[2,3] uniform pore sizes,[1] easy functionalization,[4] high porosity[5] and chemical stability.[6,7] The synthesis of continuous, thin MOF films on solid substrates opened the door for applications in membranes,[8] sensors[9] and low-κ dielectrics.[10] It is therefore not surprising that different synthesis methods have recently been developed for the preparation of MOF films.[9]

Strategies such as the solvothermal synthesis from a mother solution,[11] layer-by-layer deposition,[12] the use of stable precursor solutions[13] or galvanic displacement[14] have successfully been employed for thin film synthesis. A major disadvantage of many of these methods remains the large amounts of waste that are generated during the synthesis, especially considering the used metal salts. In order to avoid large amounts of waste, the risks and costs associated with anions such as nitrates and chlorides, respectively, oxidation and corrosion hazards, an electrochemical synthesis method was proposed.[15] This method was pioneered for copper-based MOF materials ($Cu_3(BTC)_2$), but most recently, a number of different metal electrodes (Al, Zn, Fe) were successfully used.[16,17] The method is based on the dissolution of a metallic anode and the subsequent release of metal ions into a solution containing the organic linker. By carefully modifying the synthesis conditions, films consisting of one-crystal thick layers can be synthesised. Notably, the filling of gaps in the coating to yield a continuous film seems to be an intrinsic property of electrochemical MOF growth, as the exposed metal substrate serves as a building block reservoir rather than just as a possible anchoring point.[18] Electrochemical synthesis also offers very short synthesis times, ranging from several seconds up to a few minutes in non-toxic solvents like ethanol and water.[18]

Given the recent research focus on the preparation of MOF films, it is remarkable how little is known about film mechanical behaviour or film-to-substrate adhesion strength, which are important aspects when considering practical applications. For example, in stress-induced chemical sensors, such as microcantilevers, film stiffness (Young's modulus) and film-to-substrate adhesion are key mechanical parameters that affect the attainable detection limit.[19] Until now, the mechanical properties of MOFs have only sparsely been investigated. However, recent studies allow more insight into the elastic properties of these hybrid materials.[20–25] The mechanical response of MOFs when subjected to loads below the material yield strength leads to small reversible deformations or elastic

[a]Centre for Surface Chemistry and Catalysis (COK), KU Leuven, Arenbergpark 23, B-3001 Leuven, Belgium. E-mail: dirk.devos@biw.kuleuven.be; Fax: +32 16 32 19 98; Tel: +32 16 32 16 10

[b]Department of Engineering Science, University of Oxford, Parks Road, OX1 3PJ, Oxford, UK. E-mail: jin-chong.tan@eng.ox.ac.uk; Fax: +44 (0)1865 273906; Tel: +44 (0)1865 273925

† Electronic supplementary information (ESI) available: Additional Fig. S1–S7, thin film and powder XRD diffractograms (Fig. S8–S13). See DOI: 10.1039/c3tc31039f

strains. By using a nanoindenter, this load–deformation relationship can be determined, allowing for the calculation of the corresponding elastic modulus (E) (or Young's modulus) and the hardness (H) of single crystals and films.[20] The values obtained from single crystals show that MOFs and hybrid framework materials can exhibit dramatically different mechanical properties (especially E and H), spanning the range of organic polymers, ceramics and metallic materials.[20]

However, most studies focus mainly on indentations of single crystals;[23–25] only two studies have briefly touched on the mechanical properties of MOF-films.[10,24] Bundschuh *et al.*[24] performed an indentation study on the (100) plane of an epitaxially grown film of $Cu_3(BTC)_2$ to obtain the corresponding Young's moduli and hardness ($E_{(100)} = 9.3$ GPa and $H_{(100)} = 0.20$ GPa). The solvothermal method employed by Eslava *et al.*[10] resulted in ZIF-8 films without preferential crystal facets on the film surface (*i.e.* textureless). In this case, E and H were obtained by assuming the presence of a randomly-oriented crystal facet on the film surface, resulting in an average value of Young's modulus and hardness to be measured *via* the indentation experiment ($E = 3.5$ GPa and $H = 0.43$ GPa).

In this work, the mechanical properties of three different electrochemical Cu-MOF coatings have been investigated in detail. For the first time, $Cu(INA)_2$ and Cu(CHDA), constructed from isonicotinic acid (INA)[27] and *trans*-1,4-cyclohexanedicarboxylic acid (CHDA),[28] respectively, were electrochemically synthesised as densely packed coatings. The coatings were subjected to nanoindentation measurements to determine the values of E and H. In addition, nanoscratch tests have been conducted for the first time on MOF-films. It should be noted that the resistance of a MOF-film to abrasion and scratching is of high importance considering the stresses and strains such coatings would have to sustain in real-life applications. Nanoscratching is already a well-known technique for characterising the wear resistance of materials such as ceramics, oxides, metals and organic polymers.[29–33] Furthermore, nanoscratch experiments can provide insight into the attachment strength of the film to the substrate, by determining the applied force needed for delamination.[32]

2 Experimental

2.1 Electrochemical synthesis of MOF coatings

In 100 ml of solvent mixtures of EtOH–H_2O with different ratios, 5.8 mmol of the ligand (1,3,5-benzenetricarboxylic acid, *trans*-1,4-cyclohexanedicarboxylic acid or isonicotinic acid) was dissolved and stirred until a clear solution was obtained. To this, a mixture of 6.42 mmol of tributylmethylammonium methyl sulfate (MTBS) was added, which serves as a conduction salt during the electrochemical synthesis. The clear solution was heated to 328 K and pure copper electrodes (3 cm × 1 cm × 2 mm) spaced 1 cm apart were partially immersed in the solution. By applying a chosen voltage (1–30 V), MOF-films were grown on the anode under static conditions. After the required synthesis time (ranging from 1 to 180 s), the coatings were washed with ethanol to remove the unreacted ligand and Cu^{2+} ions.

2.2 Characterization

Powder XRD patterns were recorded on a STOE STADI P Combi instrument in the Debye–Scherrer geometry (Cu Kα1) using an IP position-sensitive detector ($2\theta = 0$–$60°$; $\Delta 2\theta = 0.03°$). Film XRD patterns were recorded on a STOE STADI MP in the Bragg–Brentano mode (2θ–θ geometry; Cu Kα1) using a linear position-sensitive detector: step width of 0.5° 2θ ($2\theta = 5$–$40°$; $\Delta 2\theta = 0.01°$). Scanning electron micrographs of MOF coatings on pure copper electrodes were recorded on either Au-coated samples using a Philips XL30 FEG microscope or on non-coated samples using a Carl Zeiss Evo LS15 environmental SEM.

2.3 Nanoindentation and nanoscratch experiments

Nanoindentation experiments were performed using an MTS Nanoindenter equipped with the DCM II head (Dynamic Contact Module II). Indentations were conducted under the displacement-controlled CSM mode (Continuous Stiffness Measurement), so that the values of E and H can be determined as a function of the surface penetration depth. A 2 nm sinusoidal displacement at 45 Hz was superimposed onto the system's primary loading signal, and the loading and unloading strain rates were set at 5×10^{-2} s^{-1}. All tests were performed with a maximum indentation depth of 1000 nm using a Berkovich diamond tip. The raw data (load–displacement curves) obtained were analysed assuming a Poisson's ratio of 0.18 and by using the Oliver and Pharr method.[34] A typical load–displacement curve is presented in Fig. S1.† The nanoscratch tests were performed on the MTS nanoindenter using the XP head. During the scratch tests, the specimen with a coated surface was laterally translated under the indenter head while maintaining a prescribed load, for a total scratch length of 50–100 μm at a speed of 5 μm s^{-1} in the 0° or 180° direction (Fig. S2†). During a ramp load scratch test (RLS), the normal load was progressively increased from 0 to 10–40 mN at a loading rate of 0.5 mN s^{-1}. The pass and return wear scratch test (PRW) has a constant load of 1 mN and each cycle consists of a pass in the 0° direction and a return in the 180° direction. For the PRW, 10 cycles were performed. For each scratch test, a set of surface profiles along the track was measured, including the track profile before scratch (Profile), during scratch (Scratch) and after scratch (Post-profile). The profiling load was set at a relatively small value of 50 μN with a profiling velocity of 1 μm s^{-1}.

2.4 Evaluation of crystallinity

To evaluate the crystallinity under increased uniaxial pressure, a literature method was followed.[35] MOF powder was pressed between two metal blocks at pressures ranging from 0 to 250 bar. The pressure was kept for 30 seconds, after which an XRD diffractogram was taken. The broadening of the diffraction peaks at low angles (5–20° 2θ) is analysed using the full width half mid-height (FWHM) calculations in OriginPro 9.0 software.

3 Results

3.1 Synthesis of MOF coatings

As could be expected from the solvothermal synthesis conditions for $Cu_3(BTC)_2$, Cu(CHDA) and $Cu(INA)_2$, the rate of nucleation and growth is different for each MOF during electrochemical deposition.[26,27,36] In order to make dense coatings, the influence of the synthesis conditions (voltage, time, *etc.*) on the coverage and thickness of the films was investigated. Carefully controlling these parameters, together with the composition of the solvent (mixtures of EtOH–H_2O in different ratios), allowed the synthesis of dense coatings of the three MOFs (Fig. 1 and S3†). Due to different formation kinetics, the size of MOF crystallites constituting the three coatings is different. While $Cu_3(BTC)_2$ has crystals up to 15 μm, the crystal size of the highly intergrown Cu(CHDA) film is around 3 μm and $Cu(INA)_2$ coatings consist of intergrown crystals smaller than 2 μm. The thickness of the coatings was evaluated by cross-section SEM (Fig. S4–S6†) and measured accordingly: 11–15 μm for $Cu_3(BTC)_2$, 1.3–1.5 μm for Cu(CHDA) and 1.6–1.9 μm for $Cu(INA)_2$. The synthesis conditions are summarised in Table S1 in the ESI.†

3.2 Indentation experiments

The stiffness of a material under an elastic strain (reversible) is denoted as the elastic modulus (E), while the hardness (H) indicates the resistance of the material towards plastic deformation (irreversible).[37] These mechanical properties of a small volume of the material are most frequently measured using indentation techniques, for which CSM is the ideal technique, especially for the mechanical property measurements of thin films.[38] In a conventional nanoindenter, the contact stiffness can be inferred from the initial unloading contact stiffness, more specifically the slope of the initial portion of the unloading curve. When using the CSM technique, contact stiffness can be extracted continuously during the loading portion of the indentation test, by superimposing a harmonic oscillation onto the nominally increasing load (Fig. S1†). This makes the CSM technique ideal for thin films and graded materials, as the elastic modulus and hardness can be monitored as a function of indentation depth.[38] As the MOF films in this study consist of randomly oriented crystallites exposing different crystal facets, a large variation in load–displacement behaviour is to be expected (Fig. S7–S9†), especially considering the anisotropy in mechanical properties of the MOF crystals and the grain boundary phenomena of the polycrystalline film.[24–26,39] The largest variation in these load–displacement curves can be found for $Cu_3(BTC)_2$, coinciding with the relatively large roughness of the $Cu_3(BTC)_2$ coating (Fig. 1). Nevertheless, these indentation experiments will give good insight into the mechanical properties of the complete film, as the indenter tip is sufficiently large (Berkovich face angle of ~142°) to indent several crystallites per indent and each film is indented more than 15 times (increasing the number of indents did not change the standard deviation significantly). In Fig. 2, the representative load–displacement curves of the three MOF-films are shown. Distinct differences are clearly observed for the load–displacement curves of the three types of materials. The load developed during the indentation of the Cu(CHDA) film reaches a maximum magnitude of ~8 mN, while for $Cu_3(BTC)_2$ and $Cu(INA)_2$, the maximum loads are ~2 mN and ~1 mN, respectively. An important property that can be derived directly from the load–displacement curves is the elastic recovery upon unloading, where the vertical displacement recorded by the unloading curve is directly proportional to the elastic recovery of the materials. They are calculated at these applied maximum

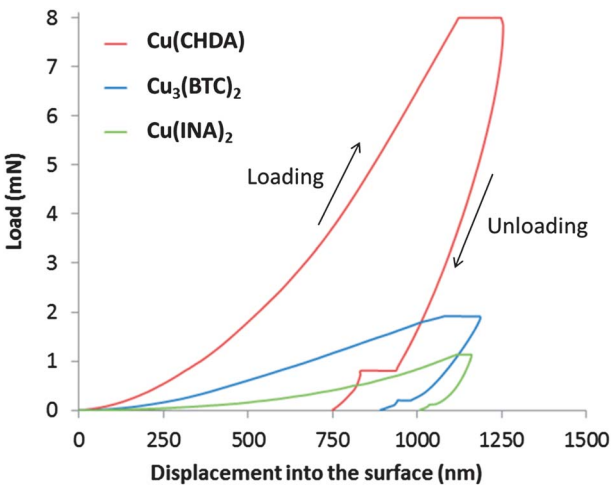

Fig. 2 Typical load–displacement curves of $Cu_3(BTC)_2$, Cu(CHDA) and $Cu(INA)_2$ films.

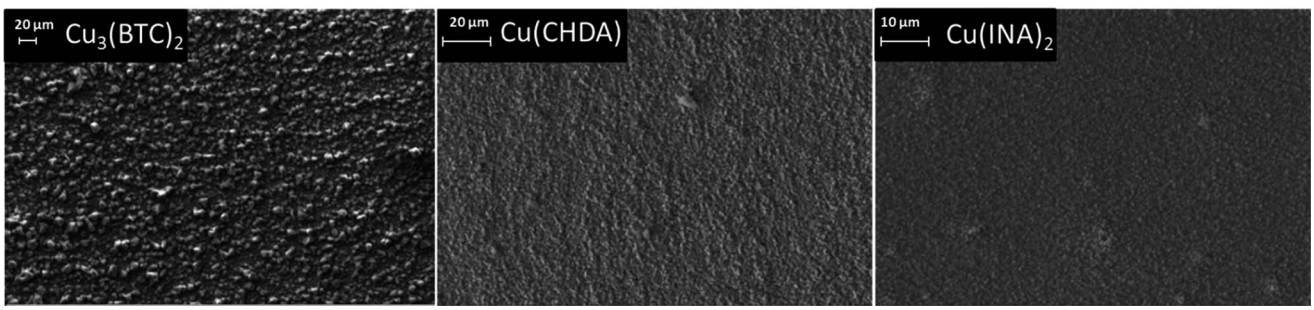

Fig. 1 Electrochemical growth of $Cu_3(BTC)_2$, Cu(CHDA) and $Cu(INA)_2$ on copper anodes.

loads to be 40% for Cu(CHDA), 25% for $Cu_3(BTC)_2$ and 14% for $Cu(INA)_2$.

Using the CSM load–displacement data, the E and H are calculated with the method of Oliver and Pharr.[34] Similar to the load–displacement curves, the largest variation in the E and H as a function of indentation depth (Fig. S10–S15†) can be found for $Cu_3(BTC)_2$, due to the surface roughness of the film. The average E and H as a function of the indentation depth of 15 indents are presented in Fig. 3 and 4. As the thickness of the MOF-coatings is only a few microns, a contribution of the Cu substrate is to be expected if the indentation is too deep. For Cu(CHDA) and $Cu(INA)_2$, the curves in Fig. 3, representing E *versus* the displacement into the surface, show an increase in E with indentation depth. This can be understood as a contribution of the underlying Cu substrate to the calculated moduli, which is absent when probing the relatively thick $Cu_3(BTC)_2$ coating. However, as the elastic modulus of the substrate (>50 GPa) is three times or more larger than the recorded values of the films, the effect of the substrate on the obtained values is expected to be quite limited. To minimise this effect, the range for the calculation of the E and H values was set from 50 to 200 nm indentation depth (Table 1).

As is clear from the nanoindentation results summarised in Table 1, substantial differences in E and H are observed for the three materials. It should be taken into account that the indentation data are collected for a polycrystalline film with different crystal orientations in which grain boundary phenomena may affect the indentation results. These considerations together with the roughness of the films are a direct explanation for the large standard deviations in mechanical properties (Table 1). Nevertheless, clear correlations can be made between the results for these different materials and their structural properties. Cu(CHDA) has the largest stiffness (E = 10.9 GPa) and hardness (H = 0.46 GPa) of the three materials. This high average stiffness and hardness can be related to the presence of rigid Cu-oxo chains running along the c-axis in the crystal lattice (Fig. S16†), leading to a relatively high crystal density of 1.49 g cm^{-3} (Table 1).

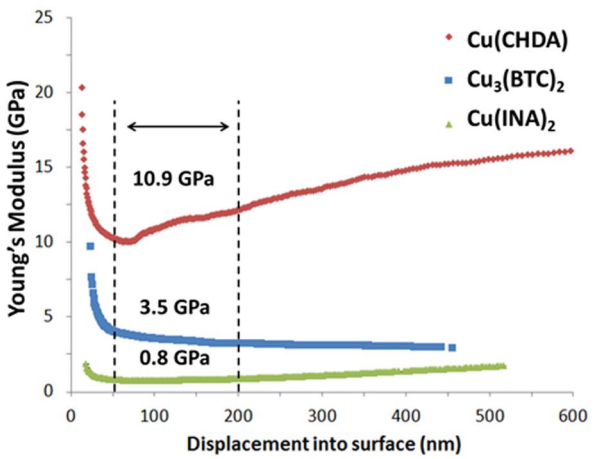

Fig. 3 The average Young's moduli as a function of indentation depth, corresponding to the 15 individual indentations with standard deviations for Cu(CHDA), Cu3(BTC)$_2$ and Cu(INA)$_2$ of 3.1, 2.5 and 0.3 GPa, respectively.

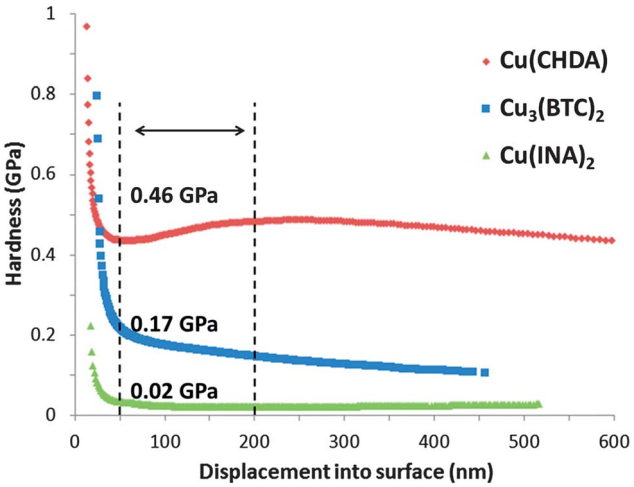

Fig. 4 The average hardness as a function of displacement into the surface, corresponding to the 15 individual indentations with standard deviations (15 measurements) for Cu(CHDA), $Cu_3(BTC)_2$ and $Cu(INA)_2$ of 0.14, 0.16 and 0.01 GPa, respectively.

Table 1 Young's modulus (E), hardness (H) and plasticity index (Ψ) of the MOF films (averaged over an indentation depth of 50–200 nm), together with the theoretical density and % solvent accessible volume (SAV corresponds to internal pore volume)

	E (GPa)[a]	H (GPa)[a]	Ψ[b]	Density[c]	SAV[d] (%)
Cu(CHDA)	10.9 ± 3.1	0.46 ± 0.14	0.63	1.49	25
$Cu_3(BTC)_2$	3.5 ± 2.5	0.17 ± 0.16	0.79	1.22	50
$Cu(INA)_2$	0.8 ± 0.3	0.02 ± 0.01	0.86	1.51	22

[a] The errors correspond to standard deviations of more than 15 measurements. [b] The plasticity index was calculated following the literature method.[31] [c] The theoretical framework densities are as given in the cif files, with the unit g cm^{-2}. [d] Solvent accessible volume (in %) is computed using the "VOID" algorithm implemented in the PLATON package.

Compared to Cu(CHDA), the stiffness (E = 3.5 GPa) and hardness (0.17 GPa) of $Cu_3(BTC)_2$ are three times smaller. Here, the E for the (randomly oriented) polycrystalline film is substantially lower compared to a previously obtained E in the study of Bundschuh *et al.* of an epitaxially grown $Cu_3(BTC)_2$ film (E = 9.3 GPa), in which only the (100) facets are indented such that no elastic anisotropic effects are taken into account. The hardness of the $Cu_3(BTC)_2$ film (H = 0.17 GPa) is, however, in good agreement with the literature value (H = 0.2 GPa).[24] This observation suggests that less anisotropy in hardness is present, which is consistent with previously published studies.[40,41]

The material with both the smallest E and H is $Cu(INA)_2$, with 0.8 and 0.02 GPa, respectively; these results are counterintuitive given that the density of the $Cu(INA)_2$ framework is indeed the highest of the three materials studied here (SAV% the lowest). Notably, our previous work on a subfamily of MOFs (termed ZIFs) has established that the elastic modulus scales with framework density and SAV%.[37] The values we obtained here for

$Cu(INA)_2$ are comparable with soft organic polymers, with *E*s ranging from 0.1 GPa up to 10 GPa and *H*s ranging from 0.01 GPa up to 0.4 GPa.[20] Such low values can be related to the physical properties and molecular structure of the framework. In particular, it is known that $Cu(INA)_2$ can exhibit an expansion-contraction of up to 10 volume% of the framework (Fig. S17†).[27] Reversible expansions of the framework under stimuli like temperature, the presence of guest molecules or pressure are known as breathing behaviour.[2,3] Because the atomic displacement can reach up to several Å, the mechanical response of the framework to an applied force is expected to be different from those of non-breathing frameworks, like Cu(CHDA) and $Cu_3(BTC)_2$. Recent theoretical studies have predicted that breathing can have a large effect on the mechanical properties, leading to very low *E*s and large anisotropies.[39] In light of this, our observations for $Cu(INA)_2$ support the idea that materials with pronounced breathing behaviour may exhibit a relatively low value of *E*. Furthermore, the very low hardness could arise from the weaker Cu–nitrogen bond compared to the Cu–oxygen bond in the other frameworks, like Cu(CHDA) and $Cu_3(BTC)_2$. However, a detailed single-crystal Brillouin scattering study accompanied by density-functional computations is needed to establish the full set of $Cu(INA)_2$ elastic constants, from which the underlying deformation mechanisms can be elucidated (for example, see ref. 22).

Additionally, in an attempt to quantify the relative plastic/elastic behaviour of the coatings, the plasticity index (Ψ) was calculated and is presented in Table 1.[31] $Cu(INA)_2$ has the highest plasticity index, followed by $Cu_3(BTC)_2$ and Cu(CHDA). The plasticity index of Cu(CHDA) (0.63) is comparable with that of organic polymer films like polymethylmethacrylate (0.6), polystyrene (0.58) and polycarbonate (0.58),[42] while the high plasticity indices of $Cu_3(BTC)_2$ (0.79) and $Cu(INA)_2$ (0.86) are comparable with those of metallic films, like stainless steel (0.89) and $Al_{12}(Fe,Cr)_3Si_2$ (0.78).[43] However, for $Cu(INA)_2$, we propose that the high plasticity index may be related to the breathing behaviour of this open-framework material, rather than to a (irreversible) plastic response alone.[39] Moreover, it is clear from these results that MOFs have plasticity indices spanning the range of organic and inorganic materials, making them a true hybrid class of materials.[1]

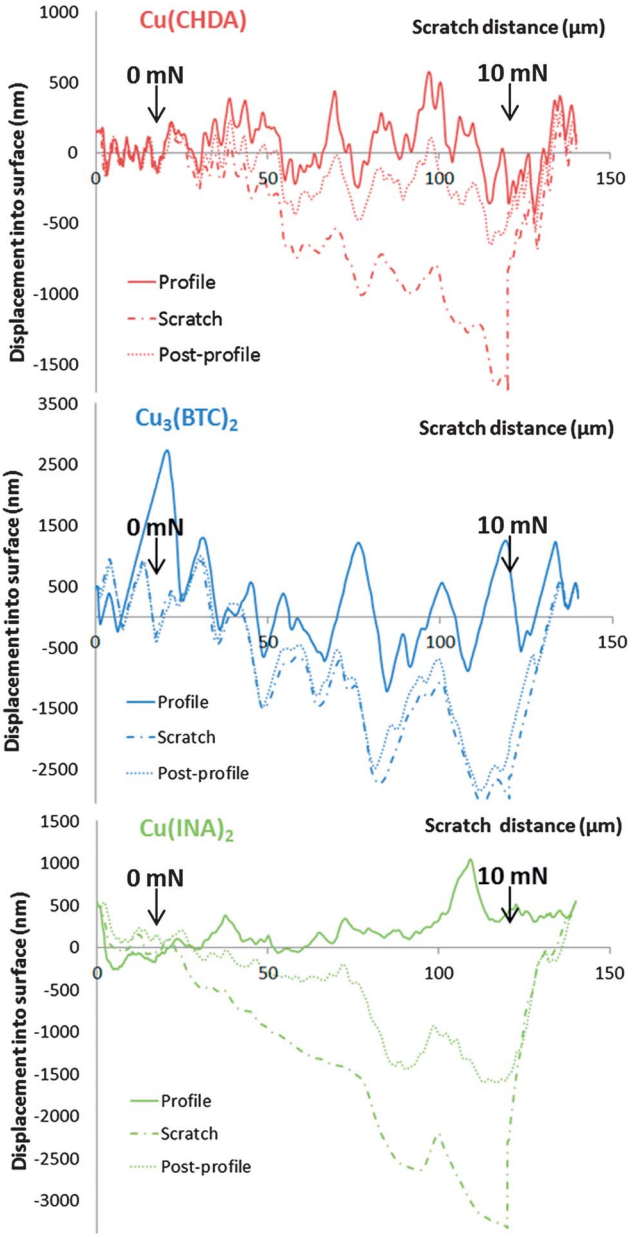

Fig. 5 Scratch profiles in the ploughing mode with the displacement into the surface as a function of the scratch distance. The load was set at 0 mN at 20 μm and increased linearly up to 10 mN at 120 μm.

3.3 Scratch experiments

In order to probe the cohesion and attachment strength of the films, nanoscratch experiments using a Berkovich indenter tip were performed. The three-faced pyramidal geometry of the indenter tip makes it possible to perform two different scratch movements (Fig. S2†), with either the sharp tip or the blunt side facing the scratching direction, hereafter referred to as ploughing and pushing, respectively.

Ramp-load scratches. In the first set of scratch experiments, the applied force was linearly increased along the scratch distance, from 0 up to 10 mN. Representative scratch profiles in the ploughing mode and pushing mode are presented in Fig. 5 and S6.† During the scratch sequence, a profile scan is performed in the direction of the scratch length. The roughness of the $Cu_3(BTC)_2$ coating is significantly larger compared to the other samples. The sharp peaks of the profiles indicate the edges of the different crystals. The roughness is therefore directly proportional to crystallite size, as can be seen in the profile scans of the coatings (Fig. 5 and S18†). The roughness after the scratch experiment was calculated for the three coatings and was independent of the scratch mode; $Cu_3(BTC)_2$ had the highest roughness, followed by Cu(CHDA) and $Cu(INA)_2$ (Table 2).

The depths at the maximum applied load, *i.e.* at the end of the scratch, for the three materials are significantly different and can be related to the mechanical properties obtained in the indentation experiments. For the two scratch modes, the results are presented in Table 2.

Table 2 The average scratch depth at maximum load (10 mN) and the residual roughness[a]

	Scratch mode	Cu(CHDA)	$Cu_3(BTC)_2$	$Cu(INA)_2$
Scratch depth	↑	1380 ± 126	2720 ± 275	3280 ± 510
	↓	1150 ± 133	1950 ± 71	1500 ± 424
Residual roughness	↑	65 ± 4	105 ± 7	35 ± 1
	↓	55 ± 1	107 ± 23	28 ± 10

[a] The scratch depth and residual roughness are presented in nm averaged over three scratches together with the calculated standard deviation.

In the ploughing mode, the material with the highest hardness, Cu(CHDA), is only penetrated up to 1380 ± 126 nm at 10 mN, while the very soft and flexible $Cu(INA)_2$ is penetrated up to 3280 ± 510 nm. Note that for Cu(CHDA) this penetration depth is indeed smaller than the thickness of the coating, while for $Cu(INA)_2$ the penetration depth is larger than the thickness of the coating, therefore exposing the underlying substrate, as evidenced in Fig. 6 in the form of coating delamination. $Cu_3(BTC)_2$, which has an intermediate hardness, also has an intermediate penetration depth of 2720 ± 275 nm. For the experiments in the pushing mode, the trend is similar, but the scratch depth is significantly smaller. Cu(CHDA) is penetrated up to 1150 ± 133 nm, $Cu_3(BTC)_2$ up to 1950 ± 71 nm and $Cu(INA)_2$ up to 1500 ± 424 nm. The use of the sharp edge in the ploughing mode results clearly in a deeper penetration depth, compared to the pushing mode.

Whilst it is well established that H is directly proportional to the resistance to scratch penetration,[31] further comparison of the scratch profile with the post-profile scan shows remarkable differences in the elastic recovery of the materials. Here, the elastic recovery is defined as the difference in scratch depth and the post-profile scan, compared to the original profile scan. For $Cu_3(BTC)_2$, very little elastic recovery is detected, as the profile depth during the scratch and the post-profile scan are very close to each other, reaching a maximum recovery of 200 nm or less than 10% of the scratch depth. For Cu(CHDA) and $Cu(INA)_2$, large elastic recoveries of more than 65% and 40%, respectively, are measured. So, even though the scratch depth in the ploughing mode for Cu(CHDA) is more than 1300 nm (elastic deformation), the residual profile is only 400 nm deep (plastic deformation). The elastic recovery of Cu(CHDA) is comparable with that of organic polymers and nanocomposites (60–80%),[44,45] while $Cu(INA)_2$ has a similar value as a scratched zeolite MFI film (37%).[46] In order to further analyse the possible loss of mechanical integrity of the MOF films, scratches were evaluated by SEM. By studying the formation of pile-ups, cracks and possible delamination, more insight into the plastic deformation can be gained.[31] Furthermore, the effect of the scratch mode is clearly visible in Fig. 6 for $Cu(INA)_2$. Delamination occurs in the ploughing mode after 40 μm (corresponding to the 4 mN applied normal force), exposing the underlying Cu-electrode (substrate). The sharp edge of the indenter tip ploughs through the coating, dislodging coating fragments up to 25 μm from the scratch (Fig. 6). The delamination suggests a poor bonding of the MOF with the substrate relative to the bonding of the particles in the coating. In contrast, when the indenter tip is set in the push mode, no delamination of the $Cu(INA)_2$ (Fig. 6), or Cu(CHDA) and $Cu_3(BTC)_2$ coatings is observed. However, a clear pile-up is detected at the end of the scratch.

Wear-track scratches. To evaluate the abrasion resistance of the coating, a scratch wear test is performed with a constant applied load for ten cycles, for which each wear cycle consists of a scratch in both the ploughing mode and the pushing mode. In order to evaluate the performance of the films, the wear track deformation is calculated as the area between the original surface profile and the tenth cycle's displacement into the surface, and is presented in Table 3 for the three materials with constant loads of 1 and 5 mN over a 50 μm wear distance. By increasing the load from 1 to 5 mN, the wear track deformation for all the coatings increases. This is to be expected considering the greater penetration depth that can be reached at the increased applied load. For Cu(CHDA) and $Cu_3(BTC)_2$, the wear track deformation doubles; for $Cu(INA)_2$, a three-fold increase is detected. Again, the same trends can be observed as for the scratch experiments: the film of Cu(CHDA) with the highest E and H has the smallest wear track deformation. Intermediate deformations are detected for $Cu(INA)_2$, while significantly larger deformations are registered for $Cu_3(BTC)_2$. In order to understand this very large wear track deformation, the accompanying SEM pictures are presented in Fig. 7, to elucidate the mechanisms taking place during the wear test. It can be seen that the large crystal size of $Cu_3(BTC)_2$ is an important factor contributing to the large wear track deformations.

Similar to the scratch tests, very large $Cu_3(BTC)_2$ crystals are easily fractured and removed from the surface in subsequent

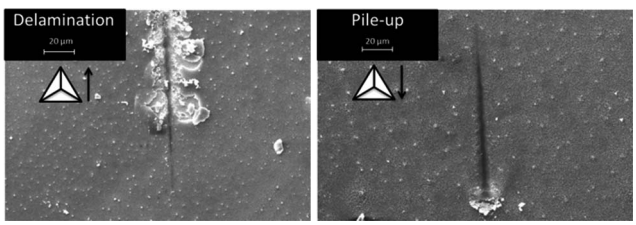

Fig. 6 SEM pictures of scratches on the $Cu(INA)_2$ coating in the ploughing mode (left) and the pushing mode (right).

Table 3 Wear track deformation[a] at a constant load of 1 or 5 mN over a wear distance of 50 μm

	Cu(CHDA)	$Cu_3(BTC)_2$	$Cu(INA)_2$
1 mN	20 ± 9	105 ± 33	29 ± 4
5 mN	42 ± 2	213 ± 13	96 ± 1

[a] The wear track deformation is presented as μm^2 ± standard deviation.

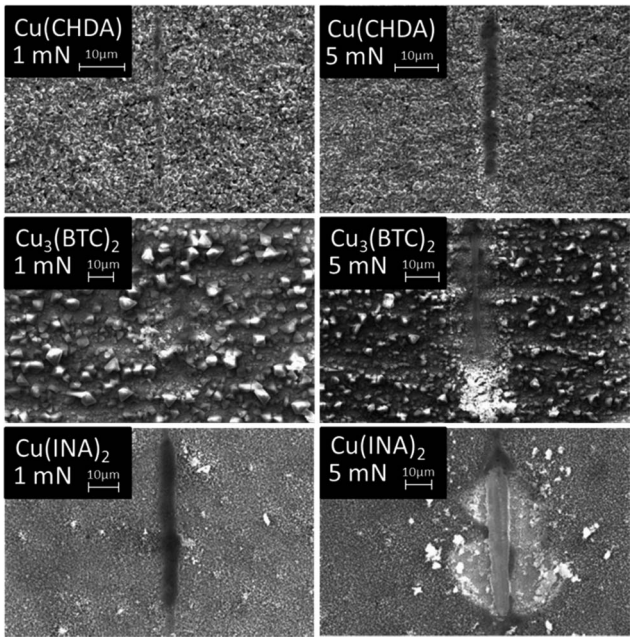

Fig. 7 SEM pictures of the wear track scratch tests on the three MOF-films, comparing a 1 mN load with a 5 mN load.

runs, thus leading to very large wear track deformations. As can be seen in Fig. 7, for $Cu_3(BTC)_2$, clear debris can be detected in the middle and at the end of the wear track, even resulting in an exposed Cu surface at a 5 mN applied force. Cu(CHDA) has almost no residual imprint after the wear test at 1 mN and no detached particles can be detected. Increasing the applied load to 5 mN leads to a clear visual wear track, but only very little debris can be seen at the end of the scratch. The very soft material, $Cu(INA)_2$, has some debris for the 1 mN wear track and very clear delamination at the 5 mN wear track. This confirms that the delamination of the $Cu(INA)_2$ coating indeed occurs at an applied force between 1 and 5 mN, as seen in the ramp-load scratches (Fig. 6).

4 Discussion

The indentation and scratch data show a clear correlation between the structural characteristics and the mechanical properties. The material with the highest E and H values, Cu(CHDA), showed excellent scratch and wear resistance amongst the MOFs being investigated here. The material with intermediate hardness and stiffness, $Cu_3(BTC)_2$, proved in the scratch experiments to be the least resistant to abrasion (Table 3) and displayed the largest plastic deformation (Fig. 5, post-profile). In order to understand this difference, the size of the crystals has to be considered. For $Cu_3(BTC)_2$, the large crystals lying in the scratch or wear path are fractured more easily as evident from SEM; some of these are subsequently being pulled out from the substrate leaving behind deep depressions which resemble plastic deformation (comparing scans after recovery in Fig. 5). In contrast, the much smaller crystals of Cu(CHDA) and $Cu(INA)_2$ are being crushed under the tip, if there is no delamination, and are then compacted evenly forming a lubricant-like protective layer preventing further scarring of the substrate surface (Fig. 7 and S19†). Once the normal load is removed, large elastic recovery is observed (Fig. 5). Looking more closely at the SEM images of the scratch tests reveals a clear crushing of the crystals under compressive loading, rather than detachment (crystal pull-out) from the substrate surface. Even if the applied force is increased up to 40 mN, no delamination and only very little pile-up in the push mode is observed (Fig. S19†).

In future applications, the structural integrity of the crystals after being subjected to external mechanical stresses is of paramount importance if the performance of the coatings is to be maintained. Therefore, we have also evaluated the crystallinity of the three MOFs as a function of the applied force, the results of which are presented in Fig. 8 with corresponding SEM micrographs taken before and after the maximum pressure treatment shown in Fig. S20.†

Again, Cu(CHDA) is structurally the most stable material, maintaining more than 80% of its crystallinity after a compression up to 250 bar. The SEM images show that the crystals of Cu(CHDA) are compressed into spherical aggregates of 10 μm. Even though the applied force is of a unilateral nature, the clusters of particles are densified into well-defined spherical aggregates. The exact mechanism leading to the formation of these spherical aggregates is not yet clear, but further experiments are conducted to unravel this peculiar behaviour of Cu(CHDA).

It is intriguing to see that the flexible material, $Cu(INA)_2$, preserves up to 70% of its crystallinity, despite its relatively low E and H values obtained by nanoindentation. Nevertheless, a fragmentation of the freshly synthesised cubic crystals is observed after pressurisation at 250 bar (Fig. S20†). The observed compression of the crystals at low scratch loads combined with the results in Fig. 8 indicate that at low load the crystallinity of the crystals is well preserved. The strong

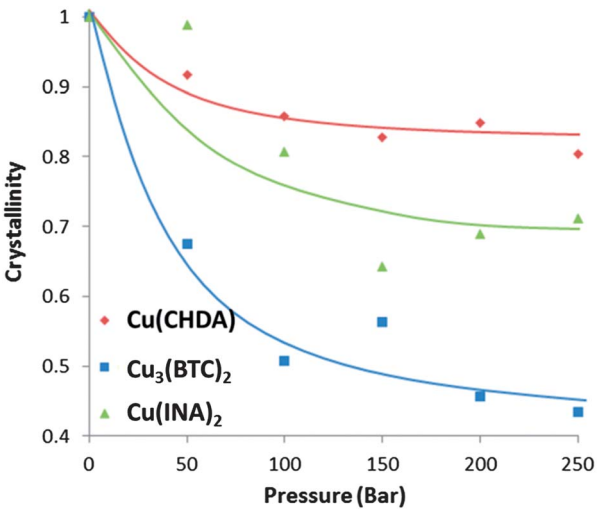

Fig. 8 The crystallinity as a function of applied pressure. The lines are guides for the eye.

cohesion between the crystals does not result in the fragmentation of the crystals in the coating but results in compression. However, if the applied force reaches a threshold value of ~4 mN, delamination of the coating is observed, suggesting that the cohesion between the crystals is stronger than the attachment strength to the surface. The low hardness and weak interaction with the Cu-surface could be due to the weaker Cu–nitrogen bond, as compared to the Cu–oxygen bonds in $Cu_3(BTC)_2$ and Cu(CHDA).

Finally, $Cu_3(BTC)_2$ loses more than 50% of its original crystallinity, coinciding with a complete loss of octahedral crystal morphology in Fig. S20.† This is in good agreement with previous studies, where the pelletisation of $Cu_3(BTC)_2$ into tablets resulted in a loss of adsorption capacity due to the high pressure treatment during the shaping process.[47,48] Thus, $Cu_3(BTC)_2$ shows a dramatic loss of crystallinity at high pressures, combined with a poor substrate attachment strength in the scratch experiments. Although no significant detachment, but rather crushing of the crystals was detected for the ramp load scratch, during the wear test even at low loads (1 mN), debris is detected at the both sides and at the end of the scratch.

5 Conclusions

Carefully controlling the synthesis conditions allowed the fabrication of electrochemically grown MOF coatings of Cu(CHDA), $Cu(INA)_2$ and $Cu_3(BTC)_2$. Furthermore, the use of nanoindentation and nanoscratch experiments proved to be an excellent combination for establishing an improved understanding of the mechanical properties of thin-film MOF coatings. While indentation has enabled the determination of elastic moduli and hardness properties, the scratch experiments have enabled us to further characterise the abrasion resistance and provide insight into the differential adhesion strength of the coatings. Cu(CHDA) proved to be the stiffest and hardest tested material, with high elastic recoveries and abrasion resistance, indicating a strong substrate attachment strength. Moreover, these properties could be linked to the structural properties of the MOF framework itself, namely the rigid Cu-oxo chain running along the *c*-axis of the crystal lattice. Additionally, we have attributed the exceedingly low Young's modulus of $Cu(INA)_2$ to the flexible nature of its framework with breathing behaviour, while its low hardness is due to the weaker coordination bonding of the pyridine ring, which is anticipated to be more susceptible to bond breakage compared with stronger ionic and covalent bonding.

Acknowledgements

D.D.V. is grateful to KU Leuven for support in the Methusalem grant CASAS, to IAP 7/05 (Belgium), to IWT (MOFShape) and FWO (K201513N and research projects). We wish to thank Professor Steve Roberts and Dr David Armstrong in the Department of Materials at Oxford University for giving us access to the nanoindenters.

Notes and references

1 L. R. MacGillivray, *Metal–Organic Frameworks: Design and Application*, Wiley, 2010.
2 T. Loiseau, C. Serre, C. Huguenard, G. Fink, F. Taulelle, M. Henry, T. Bataille and G. Férey, *Chem.–Eur. J.*, 2004, **10**, 1373–1382.
3 B. Van de Voorde, A. Munn, N. Guillou, F. Millange, D. E. De Vos and R. I. Walton, *Phys. Chem. Chem. Phys.*, 2013, **15**, 8606–8615.
4 B. Kesanli and W. Lin, *Coord. Chem. Rev.*, 2003, **246**, 305–326.
5 B. Chen, M. Eddaoudi, T. M. Reineke, J. W. Kampf and O. M. Yaghi, *J. Am. Chem. Soc.*, 2000, **122**, 11559–11560.
6 K. S. Park, Z. Ni, A. P. Côté, J. Y. Choi, R. Huang, F. J. Uribe-Romo, H. K. Chae, M. O'Keeffe and O. M. Yaghi, *Proc. Natl. Acad. Sci. U. S. A.*, 2006, **103**, 10186–10191.
7 V. Guillerm, F. Ragon, M. Dan-Hardi, T. Devic, M. Vishnuvarthan, B. Campo, a. Vimont, G. Clet, Q. Yang, G. Maurin, G. Férey, a. Vittadini, S. Gross and C. Serre, *Angew. Chem., Int. Ed.*, 2012, **51**, 9267–9271.
8 H. Bux, C. Chmelik, R. Krishna and J. Caro, *J. Membr. Sci.*, 2011, **369**, 284–289.
9 O. Shekhah, J. Liu, R. a. Fischer and C. Wöll, *Chem. Soc. Rev.*, 2011, **40**, 1081–1106.
10 S. Eslava, L. Zhang, S. Esconjauregui, J. Yang, K. Vanstreels, M. R. Baklanov and E. Saiz, *Chem. Mater.*, 2013, **25**, 27–33.
11 S. Hermes, F. Schröder, R. Chelmowski, C. Wöll and R. a. Fischer, *J. Am. Chem. Soc.*, 2005, **127**, 13744–13745.
12 O. Shekhah, H. Wang, S. Kowarik, F. Schreiber, M. Paulus, M. Tolan, C. Sternemann, F. Evers, D. Zacher, R. a. Fischer and C. Wöll, *J. Am. Chem. Soc.*, 2007, **129**, 15118–15119.
13 R. Ameloot, E. Gobechiya, H. Uji-i, J. a. Martens, J. Hofkens, L. Alaerts, B. F. Sels and D. E. De Vos, *Adv. Mater.*, 2010, **22**, 2685–2688.
14 R. Ameloot, L. Pandey, M. Van der Auweraer, L. Alaerts, B. F. Sels and D. E. De Vos, *Chem. Commun.*, 2010, **46**, 3735–3737.
15 U. Mueller, H. Puetter, M. Hesse, and H. Wessel, WO 2005/049892A1, 2005.
16 A. M. Joaristi, J. Juan-alcan, P. Serra-crespo, F. Kapteijn and J. Gascon, *Cryst. Growth Des.*, 2012, **12**, 3489–3498.
17 N. Campagnol, T. Van Assche, T. Boudewijns, J. Denayer, K. Binnemans, D. De Vos and J. Fransaer, *J. Mater. Chem. A*, 2013, **1**, 5827.
18 R. Ameloot, L. Stappers, J. Fransaer, L. Alaerts, B. F. Sels and D. E. De Vos, *Chem. Mater.*, 2009, **21**, 2580–2582.
19 A. Venkatasubramanian, J.-H. Lee, V. Stavila, A. Robinson, M. D. Allendorf and P. J. Hesketh, *Sens. Actuators, B*, 2012, **168**, 256–262.
20 J. C. Tan and A. K. Cheetham, *Chem. Soc. Rev.*, 2011, **40**, 1059–1080.
21 J.-C. Tan, P. J. Saines, E. G. Bithell and A. K. Cheetham, *ACS Nano*, 2012, **6**, 615–621.
22 J.-C. Tan, B. Civalleri, C.-C. Lin, L. Valenzano, R. Galvelis, P.-F. Chen, T. D. Bennett, C. Mellot-Draznieks, C. M. Zicovich-Wilson and A. K. Cheetham, *Phys. Rev. Lett.*, 2012, **108**, 095502.

23 T. D. Bennett, J.-C. Tan, S. a. Moggach, R. Galvelis, C. Mellot-Draznieks, B. a. Reisner, a. Thirumurugan, D. R. Allan and A. K. Cheetham, *Chem.–Eur. J.*, 2010, **16**, 10684–10690.
24 S. Bundschuh, O. Kraft, H. K. Arslan, H. Gliemann, P. G. Weidler and C. Wöll, *Appl. Phys. Lett.*, 2012, **101**, 101910.
25 K. Zagorodniy, G. Seifert and H. Hermann, *Appl. Phys. Lett.*, 2010, **97**, 251905.
26 D. Bahr, J. Reid, W. Mook, C. Bauer, R. Stumpf, a. Skulan, N. Moody, B. Simmons, M. Shindel and M. Allendorf, *Phys. Rev. B: Condens. Matter Mater. Phys.*, 2007, **76**, 184106.
27 J. Y. Lu and A. M. Babb, *Chem. Commun.*, 2002, 1340–1341.
28 H. Kumagai, M. Akita-tanaka, K. Inoue, K. Takahashi, R. Loess, L. D. C. De Coordination, L. Pasteur, I. Le Bel, B. Pascal and S. Cedex, *Inorg. Chem.*, 2007, **46**, 5949–5956.
29 J. L. Hay, R. L. White, B. N. Lucas and W. C. Oliver, *Mater. Res. Soc. Symp. Proc.*, 1998, **505**, 325–330.
30 R. D. Misra, R. Hadal and S. Duncan, *Acta Mater.*, 2004, **52**, 4363–4376.
31 H. Yahyaei and M. Mohseni, *Tribol. Int.*, 2013, **57**, 147–155.
32 F. Mammeri, E. Le Bourhis, L. Rozes and C. Sanchez, *J. Eur. Ceram. Soc.*, 2006, **26**, 259–266.
33 E. Frutos, A. Cuevas, J. L. Gonzalez-carrasco and F. Martin, *J. Mech. Behav. Biomed. Mater.*, 2012, **16**, 1–8.
34 W. C. Oliver and G. M. Pharr, *J. Mater. Res.*, 2003, **19**, 3–20.
35 V. Guillerm, F. Ragon, M. Dan-hardi, T. Devic, M. Vishnuvarthan, B. Campo, M. Daturi, G. Clet, Q. Yang, G. Maurin, G. Férey, A. Vittadini, S. Gross and C. Serre, *Angew. Chem., Int. Ed.*, 2012, **51**, 9267–9271.
36 S. S. Chui, S. M. Lo, J. P. H. Charmant, A. G. Orpen and I. D. Williams, *Science*, 1999, **283**, 1148–1150.
37 J. C. Tan, T. D. Bennett and A. K. Cheetham, *Proc. Natl. Acad.Sci. U. S. A.*, 2010, **107**, 9938–9943.
38 X. Li and B. Bhushan, *Mater. Charact.*, 2002, **48**, 11–36.
39 A. U. Ortiz, A. Boutin, A. H. Fuchs and F.-X. Coudert, *Phys. Rev. Lett.*, 2012, **109**, 195502.
40 W. Li, M. S. R. N. Kiran, J. L. Manson, J. a. Schlueter, A. Thirumurugan, U. Ramamurty and A. K. Cheetham, *Chem. Commun.*, 2013, **49**, 4471.
41 J. C. Tan, J. D. Furman and A. K. Cheetham, *J. Am. Chem. Soc.*, 2009, **131**, 14252–14254.
42 J. B. Briscoe, L. Fiori and E. Pelillo, *J. Phys. D: Appl. Phys.*, 1998, **31**, 2395–2405.
43 E. Frutos, A. Cuevas, J. L. Gonzalez-carrasco and F. Martin, *J. Mech. Behav. Biomed. Mater.*, 2012, **16**, 1–8.
44 A. Chafidz, I. Ali, M. E. A. Mohsin, R. Elleithy and S. Al-Zahrani, *J. Polym. Res.*, 2012, **19**, 9906.
45 H. Yari, S. Moradian, N. Tahmasebi and M. Arefmanesh, *Tribol. Lett.*, 2012, **46**, 123–130.
46 N. Lauridant, T. J. Daou, G. Arnold, H. Nouali, J. Patarin and D. Faye, *Microporous Mesoporous Mater.*, 2013, **172**, 36–43.
47 M. G. Plaza, A. F. P. Ferreira, J. C. Santos, A. M. Ribeiro, U. Müller, N. Trukhan, J. M. Loureiro and A. E. Rodrigues, *Microporous Mesoporous Mater.*, 2012, **157**, 101–111.
48 M. G. Plaza, A. M. Ribeiro, A. Ferreira, J. C. Santos, U.-H. Lee, J.-S. Chang, J. M. Loureiro and A. E. Rodrigues, *Sep. Purif. Technol.*, 2012, **90**, 109–119.

